

Ultrafast visualization of an electric field under the Lorentz transformation

Received: 28 December 2021

Accepted: 22 August 2022

Published online: 20 October 2022

 Check for updates

Masato Ota¹, Koichi Kan²✉, Soichiro Komada³, Youwei Wang^{1,4},
Verdad C. Agulto¹ , Valynn Katrine Mag-usara¹ , Yasunobu Arikawa¹,
Makoto R. Asakawa⁴, Youichi Sakawa¹, Tatsunosuke Matsui¹  ³ and
Makoto Nakajima¹  ✉

In special relativity, four-vectors, such as space–time, energy–momentum and electromagnetic potential vectors, follow the Lorentz transformation. The transformations of space–time and energy–momentum vectors have been tested by time dilation and rest mass energy experiments, respectively. However, the Lorentz transformation of electromagnetic potentials has never been directly demonstrated in experiments due to the limitations of the diagnostics. Here we show the spatiotemporal electric-field profiles around a highly energetic electron beam with a subpicosecond temporal resolution obtained by a terahertz technique based on electro-optic sampling. We observe the Coulomb field contraction in the propagation direction of the beam under the Lorentz transformation. After passing the beam through a metallic plate, we investigate the birth of the Coulomb field around it and follow the spatiotemporal evolution of the spherical wavefront, which is derived by the Liénard–Wiechert potentials. The measured electric-field profile in the far propagation distance is experimentally confirmed to coincide with the calculation of the Liénard–Wiechert potentials and the Lorentz transformation. Our ultrafast measurement of a spatiotemporal relativistic electric field provides both additional experimental evidence of special relativity and a platform for detailed experimental research of energetic charged particle beams and electromagnetic radiation physics.

The theory of relativity demands that we treat space and time equally. Here, a counterintuitive phenomenon occurs—distortion of space and time. However, nobody doubts the validity of this theory today, because relativity has been experimentally tested for more than a century and has become a basis of modern physics. General relativity (GR)¹, which considers the effect of gravity, has been explored through astronomical phenomena^{2–7} and by using advanced science and technology^{8–10}. On the other hand, experimental investigations of special relativity¹¹ (SR), which does not include the effect of gravity, have been limited to

a few research topics such as time dilation (for example, cosmic-ray muon lifetime¹² and clock comparison experiments^{13,14}) and relativistic energy–momentum relation (for example, nuclear fission¹⁵ and particle accelerator¹⁶) experiments. SR predicts a contraction of the Coulomb field around a charged particle moving uniformly with high velocity¹⁷ (Supplementary Fig. 1). This characteristic electric-field profile under the Lorentz transformation (LT), where we assume the Lorenz gauge, can also be derived by the Liénard–Wiechert potentials (LWPs). The LWPs predict that the wavefront of the Coulomb field around the

¹Institute of Laser Engineering, Osaka University, Suita, Japan. ²Institute of Scientific and Industrial Research (SANKEN), Osaka University, Suita, Japan.

³Department of Electrical and Electronic Engineering, Mie University, Tsu, Japan. ⁴Faculty of Engineering Science, Kansai University, Suita, Japan.

✉ e-mail: nakajima.makoto.ile@osaka-u.ac.jp; koichi81kan@gmail.com

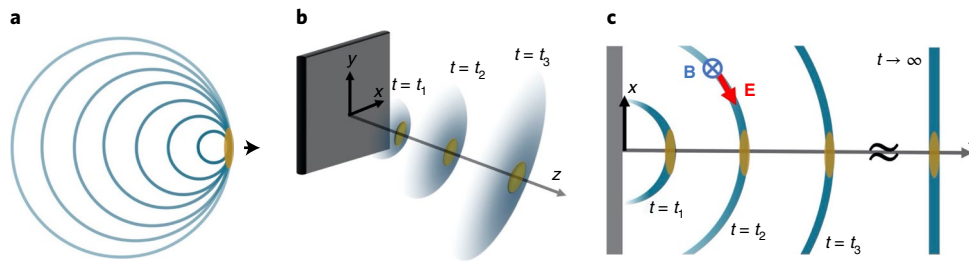


Fig. 1 | Liénard-Wiechert potentials. **a**, The generation mechanism of the spherical electromagnetic wavefront is explained by the superposition of the multiple spherical electromagnetic potentials (the blue-green circles) generated from the moving electron beam (the yellow ellipsoid). Here, the electromagnetic potentials are emitted consecutively in all directions (solid angle of 4π) at the position through which the beam propagated; they overlap in the propagation direction of the beam (forward side). This mechanism requires the beam to travel near the speed of light in a vacuum. **b, c**, Schematics of the LWP in 3D (**b**) and 2D

(**c**) space, respectively, in an inertial system. Both schematics in 3D and 2D show the evolution of the spherical electromagnetic potentials around a relativistic electron beam at times $t = t_1, t_2$ and t_3 ($t_1 < t_2 < t_3$) after the beam has passed through a metallic boundary (grey plate). The wavefront can be considered to be flat at $t \rightarrow \infty$, as shown in **c**. Here, the beam propagates along the z direction at nearly the speed of light. In **c**, vectors **E** and **B** represent the electric field and magnetic field of the electromagnetic wave derived by the LWP, respectively, at $t = t_2$. These vectors have axial symmetry around the z axis.

moving electron is derived by the integration of multiple retarded spherical electromagnetic potentials (that is, the spatiotemporal differentiation of the scalar potential and vector potential) propagating at the speed of light, as illustrated in Fig. 1a. The spherical curvature of the electric-field wavefront due to the passage of the boundary that causes the electric-field cancellation can be ignored at infinity. This is shown in Fig. 1b,c, where an electric field derived by the spatiotemporal differentiation of the LWP asymptotically coincides with the one of the LT around the electron-beam axis in the long propagation distance (that is, $t \rightarrow \infty$ in Fig. 1c): the contracted relativistic Coulomb field points radially with respect to the instantaneous position. In this Article we discuss relativistic electrons without any accelerations, and the radiation field is not considered, but the Coulomb field is.

Energetic electrons artificially generated at accelerators and naturally generated in the Universe have been utilized for experimental research on the relativistic radiation field, for example, in free-electron lasers¹⁸ and relativistic beaming¹⁹. However, here has been very little experimental research on the Coulomb field around relativistic electrons. This is mainly because the radiation field propagates a long distance, whereas the Coulomb field does not. The latter thus demands near-field ultrafast (subpicosecond) measurements. An application of electro-optic (EO) sampling^{20–23} (Methods; often utilized in ultrafast terahertz spectroscopy^{20–28}) to relativistic electron beams began in 2000, and temporal evolution of the relativistic Coulomb field was obtained with high temporal resolution, with the LT of the electromagnetic potential implicitly assumed to be valid²⁹. Here we present spatiotemporal images of the electric field around a relativistic electron beam, obtained by EO sampling. The experimental results are divided into two categories: measurements of the Coulomb-field contraction and measurements of the spatiotemporal evolution of a spherical wavefront of the Coulomb field. The former demonstrates the LT of electromagnetic potentials around a charged particle, where the boundary condition is ignored, and the latter demonstrates the generation process of the electric field under the LT, considering the boundary condition, that is, the LWP for the Coulomb field. The results of such measurements are one of the most decisive experimental proofs of SR in electromagnetism.

We measured the spatiotemporal electric-field profile around an electron beam with an energy of 35 MeV (with Lorentz factor $\gamma = 69.5$), pulse width of 0.72 ps (full-width at half-maximum, FWHM), beam diameter of 3.5 mm (FWHM) and charge of 70 pC generated by a photocathode linear accelerator (linac) (Supplementary Section 3) by EO sampling in air. For this purpose, a 1-mm-thick zinc telluride (ZnTe) crystal (110) with dimensions of 11 mm \times 10 mm was placed 204 mm from the Ti window that served as the exit of the acceleration tube.

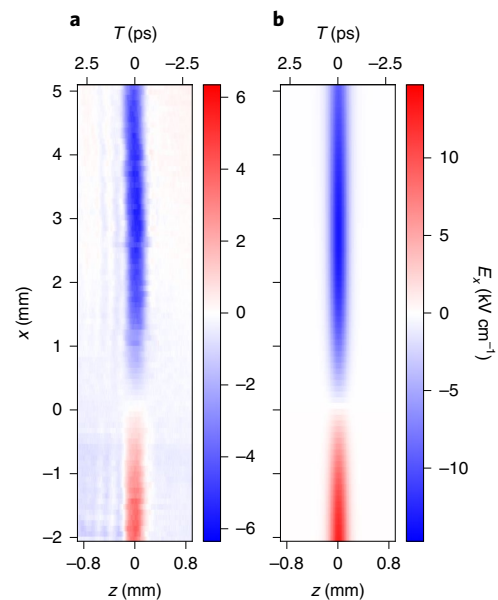


Fig. 2 | Electric-field contraction. **a, b**, Spatiotemporal transverse electric-field (E_x) profiles around a relativistic electron bunch obtained by an echelon-based single-shot measurement (**a**) and by theoretical calculation (**b**), respectively. The colour bar denotes the transverse electric-field strength.

We define the distance between the window and the ZnTe surface as D . The cancellation of the electric field because of passage through the window causes a spherical curvature of the wavefront, as shown in Fig. 1b,c. However, the propagation distance of 204 mm is sufficiently long for the curvature around the beam axis to be ignored, as discussed later in this Article. Therefore, the LT is applied to this case.

An echelon-based single-shot measurement (Supplementary Section 4) was used to obtain the spatiotemporal electric-field profile with high resolution. Figure 2a shows that the transverse electric field (E_x) around a relativistic electron bunch is contracted in the propagation direction of the beam because of the LT, which forms a terahertz electric-field pulse with a half-cycle. Here, a relative positional coordinate around the centre of the beam in the propagation direction Z is used as the horizontal axis corresponding to the time domain T , where $Z = z - D$ and $T = D/c - t$ (c is the speed of light, and z and t are the spatial coordinates in the propagation direction and time in a laboratory frame, respectively, as shown in Fig. 1b,c). In addition to

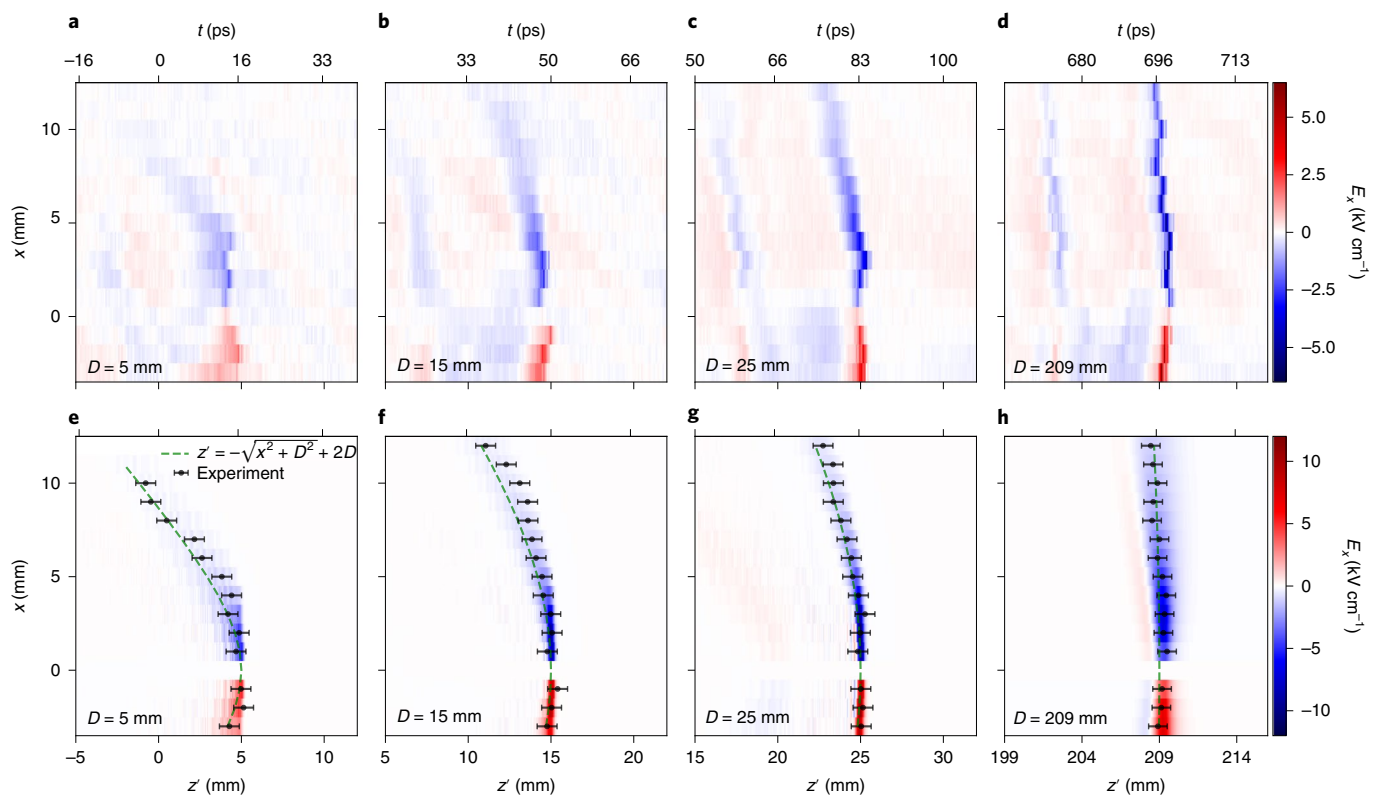


Fig. 3 | Spatiotemporal evolution of the spherical wavefront of the Coulomb field. **a–d**, Experimentally obtained spatiotemporal transverse electric-field profiles (E_x) for propagation distances (D) of 5 **(a)**, 15 **(b)**, 25 **(c)** and 209 mm **(d)** after the wavefront has passed through Al foil. In this set-up, we rotate the ZnTe by 90° around the beam axis, so the transverse direction is x , as shown in Supplementary Fig. 7. **e–h**, Simulated spatiotemporal electric-field profiles (E_x)

for D of 5 **(e)**, 15 **(f)**, 25 **(g)** and 209 mm **(h)** after the wavefront has passed through a metallic boundary. The peak positions of the electric-field strength in z' at each x in the experimental results are plotted as black circles. The error bars reflect the timing jitter (r.m.s.) between the electron beam and the probe laser (Supplementary Section 3). The green dashed curve shows the theoretically estimated peak positions: $z' = -\sqrt{x^2 + D^2} + 2D$.

the contraction, the electric field extends in the radial direction (that is, the x and y directions given the axial symmetry) and generates a plane. We note that the beam axis is at $x = y = 0$ mm and the propagation direction is positive in the Z axis. The electric field is directed towards the centre axis of the beam. Faint pulse trains were observed immediately after the electron beam passed through the ZnTe crystal ($-0.8 \text{ mm} < Z < -0.2 \text{ mm}$). This phenomenon is ascribed to the phase mismatch between a part of the terahertz waves and the probe laser because of a transverse-acoustic phonon absorption effect at 1.6 THz (ref. ³⁰). Although a part of the electron beam collides with the ZnTe (the beam axis on the ZnTe crystal is 1 mm from the outer edge), the irradiation effect can hardly be observed in this terahertz electric-field pulse signal at $Z = 0$ mm. This result is confirmed by a measurement of the terahertz electric field with and without injecting the electron beam into the ZnTe. However, the irradiation effect appears a few picoseconds after the passage of the ZnTe, as discussed later. Figure 2b shows the theoretical calculation of the terahertz electric field derived by the LT with a numerical convolution of the beam profile in 3D (Supplementary Section 2). Here, the result of the theoretical calculation (Fig. 2b) reproduces the experimental result (Fig. 2a), although the maximum electric-field strength obtained in the experiment is about two times smaller than that of the calculation. There are a few possibilities for the cause of the underestimation of the measured electric field (Supplementary Sections 6 and 7), and we will address this issue in future works. Detailed comparisons of the electric-field-strength profile and the pulse broadening in the x direction between the experiment and the calculation are shown in Supplementary Fig. 8. A large difference is observed between the electron-beam sizes in the longitudinal

(0.72 ps, or 0.22 mm) and transverse (3.5 mm) directions. This difference implies that the observed shrinkage of the electric field also demonstrates that the longitudinal beam size of the electron beam itself is shortened by a factor of 69.5 ($= \gamma$) (that is, the space–time Lorentz contraction).

So far, we have examined a simple case where the curvature of the electromagnetic wavefront around the beam axis can be regarded as a plane. Here we discuss a more general case where the curvature is not negligible. To achieve this condition, we positioned a sheet of 15- μm -thick Al foil in front of the ZnTe’s front surface at a distance of 5, 15 or 25 mm. We created a 1-mm-diameter hole on the Al foil to let the probe laser pass through without any interaction, and the electron beam passed through the foil with negligible scattering (Supplementary Fig. 7a), hence the electric-field cancellation. With this set-up, we used a balanced detection method with two photodiodes (Supplementary Fig. 7b). The spatiotemporal electric-field profile was obtained by the delay stage and by laterally shifting the optics around the ZnTe with regard to the path of the electron beam. We chose this method so as to acquire a larger and longer spatiotemporal profile, because the counterpart of the echelon-based single-shot measurement is limited by the size of the EO crystal and by the total depth of steps on the echelon mirror. Including the case without the Al foil (the distance between the Ti window and the ZnTe was 209 mm in this experimental set-up), we measured the electric field around the electron beam at four propagation distances (D) of 5, 15, 25 and 209 mm after the electric-field cancellation.

Figure 3a–d shows the evolution of a transverse electric field (E_x) with a spherical wavefront measured at distance D after the electron

beam passes through Al foil. The electric field passing through a flat measurement plane (ZnTe) was obtained at a certain z position, so the horizontal axes are labelled as $z' (= ct)$, not z , in Fig. 3a–d, where t reflects the delay between the electron beam and the probe pulse. When the wavefront of the electric field is flat, the spatiotemporal profiles can be regarded as snapshots in space, as assumed in Fig. 2a. Despite the modified coordinate (z'), the results confirm that the spherical curvature of the terahertz electric field pulse at $D = 5, 15, 25$ and 209 mm becomes smaller with increasing propagation distance in Fig. 3a–d. This verifies the approximation of the wavefront as a flat plane near the beam axis at a long propagation distance, as in Fig. 2a ($D = 204$ mm). It is also seen that the maximum electric-field intensity increases with propagation distance; the strength at $D = 209$ mm is three times greater than that at $D = 5$ mm (red data points in Supplementary Fig. 9a–d). This trend indicates that a large part of the terahertz electric-field pulse is not coherent transition radiation³¹ from the Al foil, but the integration of the electromagnetic waves consecutively emitted by a moving electron bunch. Multiple reflections of the terahertz pulse, which is first reflected on the rear side of the ZnTe and then on the front side, are observed 21 ps after the main terahertz pulse is detected. The delay between the main terahertz pulse and the multiple reflections is the same as the estimated delay derived from the refractive index of the ZnTe in the terahertz region³². A signal due to the collision between the electron beam and the ZnTe crystal is observed a few picoseconds after the irradiation (that is, the main terahertz pulse), around the beam axis. This is observed as a long-sustained electric field with a reversed sign relative to that of the main terahertz pulse.

Figure 3e–g shows the results of a three-dimensional (3D) particle-in-cell (PIC) simulation (Methods) for comparison with the experimental results for $D = 5, 15$ and 25 mm (Fig. 3a–c). Figure 3h (for $D = 209$ mm) was obtained by PIC simulation with a cylindrical coordinate because the propagation distance was too long for a 3D simulation to be conducted; this limitation arises as a result of the computation source. The effects of the EO crystals, including multiple reflections and irradiation, were not considered in either the 3D or 2D simulations. We observe a strong coincidence between Fig. 3a–d and Fig. 3e–h. In the simulation results, we overplot the experimentally obtained peak positions of the terahertz electric-field pulse as black solid circles with error bars, and the wavefront theoretically expected to be observed by the measurement plane is shown as green dashed curves. The theoretical curve is derived from the geometrical relation under the simple assumption that the electromagnetic wavefront is a sphere in space and has a radius identical to the propagation distance. This curve is expressed as $z' = -\sqrt{x^2 + D^2} + 2D$, and the effect of the beam size is ignored (Supplementary Section 8). The theoretical curves are in good agreement with the simulation and experimental results. The quantitative comparisons of the electric-field-strength profile and the pulse broadening also show agreement between the experiment and the PIC simulation (Supplementary Fig. 9). The measured spatiotemporal electric-field profile verifies the LWP for the Coulomb field: the electromagnetic waves emitted from a relativistic electron in all directions are integrated into the propagation direction and generate a spherical wavefront with a radius identical to the propagation distance, and the electric field and the pulse width become stronger and shorter, respectively, around the beam axis with the propagation.

In summary, we have experimentally demonstrated electric-field contraction around a relativistic electron beam under the LT, as well as its generation process, with a boundary condition described by the LWP using EO sampling. The shrinkage of the electric field also implies the space–time Lorentz contraction of the electron beam itself. The echelon-based single-shot measurement is one of the simplest methods to access the ultrafast spatiotemporal electric-field profile in single-shot measurements, and it can pave the way for practical applications for the measurement of energetic charged particle beams such as electrons and positrons^{33–35} and detailed experimental research

on electromagnetic radiation (that is, the electric field described by the general LWP, which includes the acceleration of charged particles) when combined with an external magnetic field³⁶ or structured material^{37–40}.

Online content

Any methods, additional references, Nature Research reporting summaries, source data, extended data, supplementary information, acknowledgements, peer review information; details of author contributions and competing interests; and statements of data and code availability are available at <https://doi.org/10.1038/s41567-022-01767-w>.

References

- Will, C. M. The confrontation between general relativity and experiment. *Living Rev. Relativ.* **17**, 4 (2014).
- Dyson, F. W., Eddington, A. S. & Davidson, C. IX. A determination of the deflection of light by the Sun's gravitational field, from observations made at the total eclipse of May 29, 1919. *Philos. Trans. R. Soc. Lond.* **220**, 291–333 (1920).
- Einstein, A. Lens-like action of a star by the deviation of light in the gravitational field. *Science* **84**, 506–507 (1936).
- Greenstein, J. L. & Trimble, V. L. The Einstein redshift in white dwarfs. *Astrophys. J.* **149**, 283–298 (1967).
- Müller, H., Peters, A. & Chu, S. A precision measurement of the gravitational redshift by the interference of matter waves. *Nature* **463**, 926–929 (2010).
- Abbott, B. P. et al. Observation of gravitational waves from a binary black hole merger. *Phys. Rev. Lett.* **116**, 061102 (2016).
- Akiyama, K. et al. First M87 Event Horizon Telescope results. I. The shadow of the supermassive black hole. *Astrophys. J.* **875**, L1 (2019).
- Baierlein, R. Testing general relativity with laser ranging to the moon. *Phys. Rev.* **162**, 1275–1288 (1967).
- Bertotti, B., Iess, L. & Tortora, P. A test of general relativity using radio links with the Cassini spacecraft. *Nature* **425**, 374–376 (2003).
- Takamoto, M. et al. Test of general relativity by a pair of transportable optical lattice clocks. *Nat. Photon.* **14**, 411–415 (2020).
- Einstein, A. Zur Elektrodynamik bewegter Körper. *Ann. Phys.* **17**, 891–921 (1905).
- Rossi, B. & Hall, D. B. Variation of the rate of decay of mesotrons with momentum. *Phys. Rev.* **59**, 223–228 (1941).
- Reinhardt, S. et al. Test of relativistic time dilation with fast optical atomic clocks at different velocities. *Nat. Phys.* **3**, 861–864 (2007).
- Delva, P. et al. Test of special relativity using a fiber network of optical clocks. *Phys. Rev. Lett.* **118**, 221102 (2017).
- Nishina, Y., Yasaki, T., Ezoe, H., Kimura, K. & Ikawa, M. Fission products of uranium produced by fast neutrons. *Nature* **146**, 24 (1940).
- Rogers, M. M., McReynolds, W. A. & Rogers, T. F. Jr. A determination of the masses and velocities of three radium B beta-particles. *Phys. Rev.* **57**, 379–383 (1940).
- Jackson, J. D. *Classical Electrodynamics* 3rd edn (Wiley, 1998).
- Deakon, D. A. G. et al. First operation of a free-electron laser. *Phys. Rev. Lett.* **38**, 892–894 (1977).
- Sparks, W. B., Fraix-Burnet, D., Macchetto, F. & Owen, F. N. A counterjet in the elliptical galaxy M87. *Nature* **355**, 804–806 (1992).
- Auston, D. H., Cheung, K. P., Valdmanis, J. A. & Kleinman, D. A. Cherenkov radiation from femtosecond optical pulses in electro-optic media. *Phys. Rev. Lett.* **53**, 1555–1558 (1984).
- Wu, Q. & Zhang, X. C. Free-space electro-optic sampling of terahertz beams. *Appl. Phys. Lett.* **67**, 3523–3525 (1995).

22. Keiber, S. et al. Electro-optic sampling of near-infrared waveforms. *Nat. Photon.* **10**, 159–162 (2016).
 23. Nakajima, M., Takubo, N., Hiroi, Z., Ueda, Y. & Suemoto, T. Photoinduced metallic state in VO₂ proved by the terahertz pump-probe spectroscopy. *Appl. Phys. Lett.* **92**, 011907 (2008).
 24. Ohkoshi, S. et al. Magnetic-pole flip by millimeter wave. *Adv. Mater.* **32**, 2004897 (2020).
 25. Fitzky, G., Nakajima, M., Koike, Y., Leitenstorfer, A. & Kurihara, T. Ultrafast control of magnetic anisotropy by resonant excitation of 4f electrons and phonons in Sm_{0.7}Er_{0.3}FeO₃. *Phys. Rev. Lett.* **127**, 107401 (2021).
 26. Agulto, V. C. et al. Terahertz time-domain ellipsometry with high precision for the evaluation of GaN crystals with carrier densities up to 10²⁰ cm⁻³. *Sci. Rep.* **11**, 18129 (2021).
 27. Bakunov, M. I., Bodrov, S. B., Maslov, A. V. & Hangyo, M. Theory of terahertz generation in a slab of electro-optic material using an ultrashort laser pulse focused to a line. *Phys. Rev. B Condens. Matter Mater. Phys.* **76**, 085346 (2007).
 28. Matsui, T., Agrawal, A., Nahata, A. & Vardeny, Z. V. Transmission resonances through aperiodic arrays of subwavelength apertures. *Nature* **446**, 517–521 (2007).
 29. Yan, X. et al. Subpicosecond electro-optic measurement of relativistic electron pulses. *Phys. Rev. Lett.* **85**, 3404–3407 (2000).
 30. Bakker, H. J., Cho, G. C., Kurz, H., Wu, Q. & Zhang, X.-C. Distortion of terahertz pulses in electro-optic sampling. *J. Opt. Soc. Am. B* **15**, 1795–1801 (1998).
 31. Casalbuoni, S., Schmidt, B., Schmüser, P., Arsov, V. & Wesch, S. Ultrabroadband terahertz source and beamline based on coherent transition radiation. *Phys. Rev. Spec. Top. Accel. Beams* **12**, 030705 (2009).
 32. Gallot, G., Zhang, J., McGowan, R. W., Jeon, T. I. & Grischkowsky, D. Measurements of the THz absorption and dispersion of ZnTe and their relevance to the electro-optic detection of THz radiation. *Appl. Phys. Lett.* **74**, 3450–3452 (1999).
 33. Emma, P. et al. First lasing and operation of an ångstrom-wavelength free-electron laser. *Nat. Photon.* **4**, 641–647 (2010).
 34. Tajima, T. & Dawson, J. M. Laser electron accelerator. *Phys. Rev. Lett.* **43**, 267–270 (1979).
 35. Corde, S. et al. Multi-gigaelectronvolt acceleration of positrons in a self-loaded plasma wakefield. *Nature* **524**, 442–445 (2015).
 36. Uchiyama, Y., Aharonian, F. A., Tanaka, T., Takahashi, T. & Maeda, Y. Extremely fast acceleration of cosmic rays in a supernova remnant. *Nature* **449**, 576–578 (2007).
 37. Smith, S. J. & Purcell, E. M. Visible light from localized surface charges moving across a grating. *Phys. Rev.* **92**, 1069 (1953).
 38. Cook, A. M. et al. Observation of narrow-band terahertz coherent Cherenkov radiation from a cylindrical dielectric-lined waveguide. *Phys. Rev. Lett.* **103**, 095003 (2009).
 39. Kan, K. et al. Generation of terahertz waves using ultrashort electron beams from a photocathode radio-frequency gun linac. *Electron. Commun. Jpn* **99**, 22–31 (2016).
 40. Lin, X. et al. Controlling Cherenkov angles with resonance transition radiation. *Nat. Phys.* **14**, 816–821 (2018).
- Publisher's note** Springer Nature remains neutral with regard to jurisdictional claims in published maps and institutional affiliations.
- Open Access** This article is licensed under a Creative Commons Attribution 4.0 International License, which permits use, sharing, adaptation, distribution and reproduction in any medium or format, as long as you give appropriate credit to the original author(s) and the source, provide a link to the Creative Commons license, and indicate if changes were made. The images or other third party material in this article are included in the article's Creative Commons license, unless indicated otherwise in a credit line to the material. If material is not included in the article's Creative Commons license and your intended use is not permitted by statutory regulation or exceeds the permitted use, you will need to obtain permission directly from the copyright holder. To view a copy of this license, visit <http://creativecommons.org/licenses/by/4.0/>.
- © The Author(s) 2022

Methods

EO sampling

EO sampling is a powerful technique for the detection of a terahertz electromagnetic wave because it offers high temporal resolution and is non-destructive. With this method, the terahertz electric-field strength induced inside an EO crystal, which exhibits the Pockels effect, is recorded as a modulation of a probe laser's polarity. EO sampling is applied to obtain the pulse width of an electron beam propagating in accelerators^{41,42} and is generated by a laser–plasma interaction^{43–46}. The electric field around the relativistic electron beam with a picosecond pulse width can be regarded as a half-cycle terahertz pulse. The measured pulse width of the terahertz electric field corresponds to the pulse width of the electron beam, and measurement of the temporal evolution with a resolution less than 100 fs has been achieved⁴⁷.

PIC simulation

To validate the experimental results, we used the electromagnetic field analysis software CST Particle Studio (Dassault Systems), based on a PIC simulation, to simulate the 3D distribution of the electric field around a relativistic electron bunch. The density profile of the electron beam is defined by Supplementary equation (2). The pulse width, transverse beam diameter, beam energy and the charge of the electron bunch were the same as in the experiment (0.72 ps (FWHM), 3.5 mm (FWHM), 35 MeV and 70 pC, respectively). The electron bunch was emitted from a perfect electrical conductor to a vacuum. The electric-field distribution was recorded after propagation distances of 5, 15 and 25 mm from the perfect electrical conductor. The inside of the simulation box was a vacuum, and the open boundary condition was applied. In the calculation, there was no EO crystal. Axial symmetry simulation was conducted using OOPIC Pro code for a propagation distance of 209 mm, where the simulation conditions were the same as in the 3D PIC except for the dimensions and the use of a filter for the numerical Cherenkov radiation. The parameters of the simulation domain in the CST (3D PIC) are as follows: the box size is 270 mm (in the x direction) \times 80 mm (in the y direction) \times 280 mm (in the z direction), the number of grids in each direction is $362 \times 123 \times 3,320$, the time step is 200 fs, and the macro particle weight is automatically adjusted. The parameters of the simulation domain in the OOPIC (PIC in cylindrical coordinates) are as follows: the box size is 50 mm (in the x direction) \times 230 mm (in the z direction), the number of grids in each direction is $500 \times 2,300$, the time step is 50 fs, and the macro particle weight is ~ 7 fC per particle.

Data availability

The data that support the findings of this study are available from the corresponding author upon reasonable request.

Code availability

The codes that support the findings of this study are available from the corresponding author upon reasonable request.

References

- Casalbuoni, S. et al. Numerical studies on the electro-optic detection of femtosecond electron bunches. *Phys. Rev. Spec. Top. Accel. Beams* **11**, 072802 (2008).
- Steffen, B. et al. Electro-optic time profile monitors for femtosecond electron bunches at the soft X-ray free-electron laser FLASH. *Phys. Rev. Spec. Top. Accel. Beams* **12**, 032802 (2009).
- Leemans, W. P. et al. Observation of terahertz emission from a laser-plasma accelerated electron bunch crossing a plasma-vacuum boundary. *Phys. Rev. Lett.* **91**, 074802 (2003).
- Debus, A. D. et al. Electron bunch length measurements from laser-accelerated electrons using single-shot THz time-domain interferometry. *Phys. Rev. Lett.* **104**, 084802 (2010).
- Bisesto, F. et al. Novel single-shot diagnostics for electrons from laser-plasma interaction at SPARC_LAB. *Quantum Beam Sci.* **1**, 13 (2017).
- Huang, K. et al. Electro-optic spatial decoding on the spherical-wavefront Coulomb fields of plasma electron sources. *Sci. Rep.* **8**, 2938 (2018).
- Berden, G. et al. Benchmarking of electro-optic monitors for femtosecond electron bunches. *Phys. Rev. Lett.* **99**, 164801 (2007).

Acknowledgements

We acknowledge discussions with D. Li, M. Murakami and M. Nakai. This work was supported by JSPS KAKENHI grants nos. JP20H02206, JP19K05331, JP20H00364 and JP19J207650. This work was partly performed with the support and under the auspices of the NIFS Collaborative Research Program (2021NIFS18KUGK125 and 2022NIFS18KUGK125). The experiment using electron beams was performed with shared use of the Research Laboratory for Quantum Beam Science, Institute of Scientific and Industrial Research (SANKEN), Osaka University. Examination of offline tests using the ZnTe and preparation of optics were performed in the Advanced Nanotechnology Instrument Laboratory and Nanofabrication Shop (SANKEN).

Author contributions

M.O., K.K. and M.N. designed the study. M.O., K.K. and Y.W. performed the EO sampling experiments. M.O. and K.K. conducted the data analysis. K.K., S.K. and T.M. carried out the PIC simulation. M.N. supervised the project with K.K. and M.O. M.O. and M.N. wrote the paper with contributions from all authors.

Competing interests

The authors declare no competing interests.

Additional information

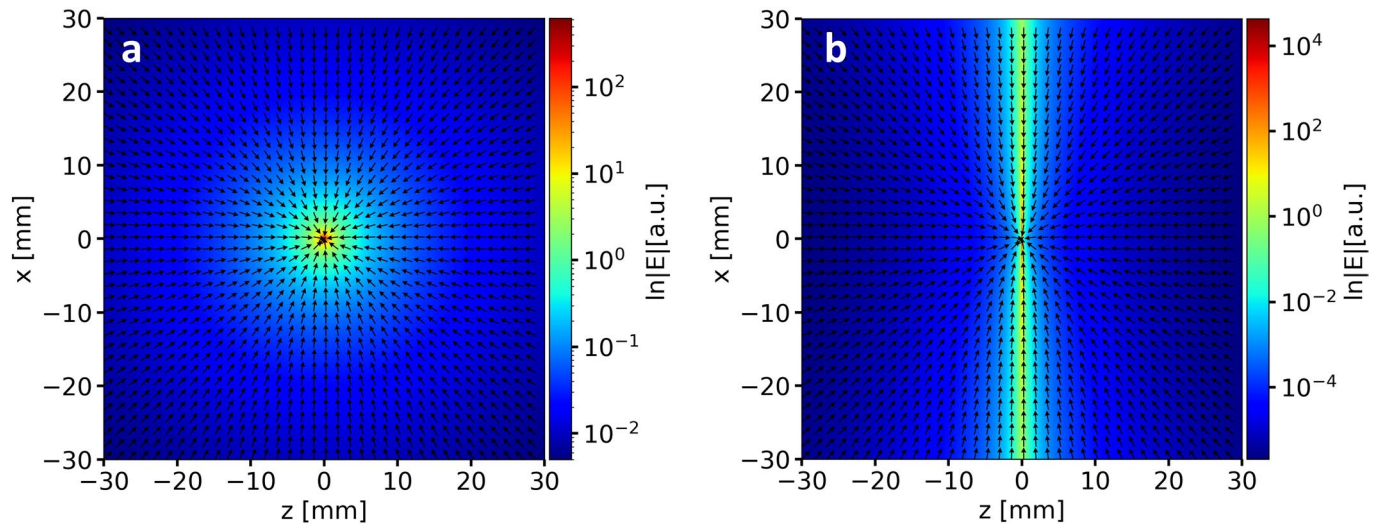
Extended data is available for this paper at <https://doi.org/10.1038/s41567-022-01767-w>.

Supplementary information The online version contains supplementary material available at <https://doi.org/10.1038/s41567-022-01767-w>.

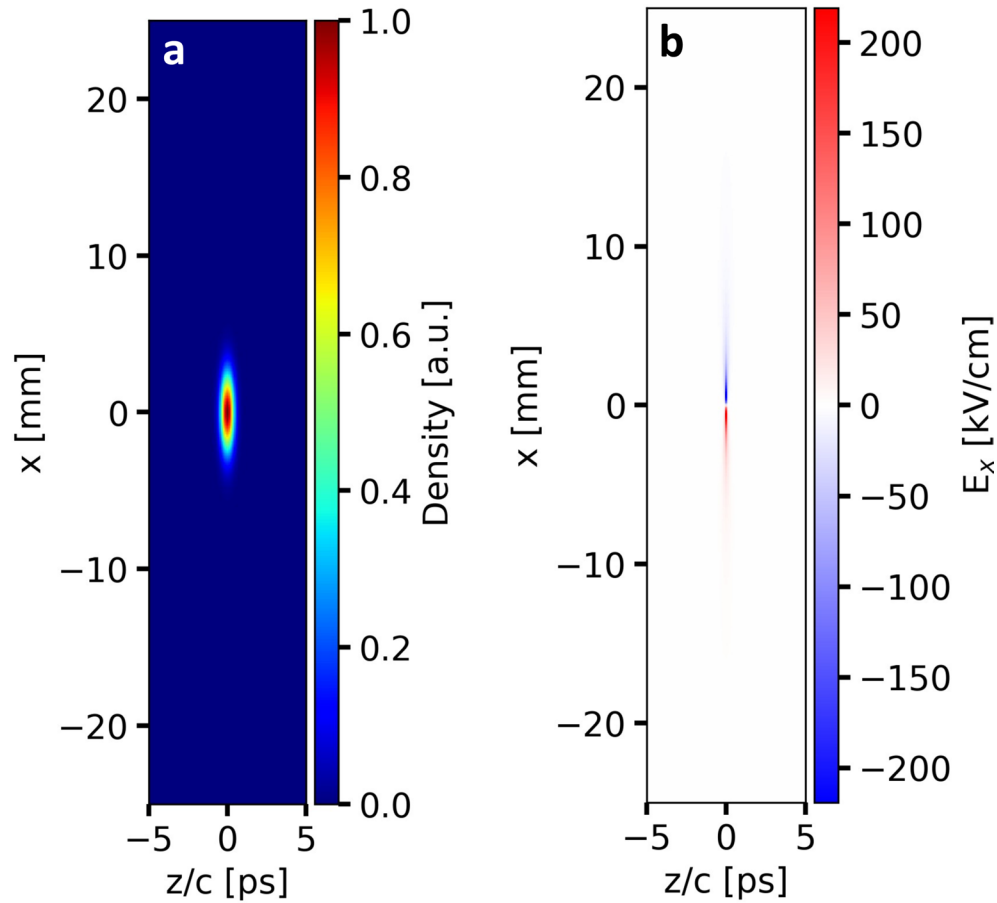
Correspondence and requests for materials should be addressed to Koichi Kan or Makoto Nakajima.

Peer review information *Nature Physics* thanks Domenico Giulini and the other, anonymous, reviewer(s) for their contribution to the peer review of this work.

Reprints and permissions information is available at www.nature.com/reprints.

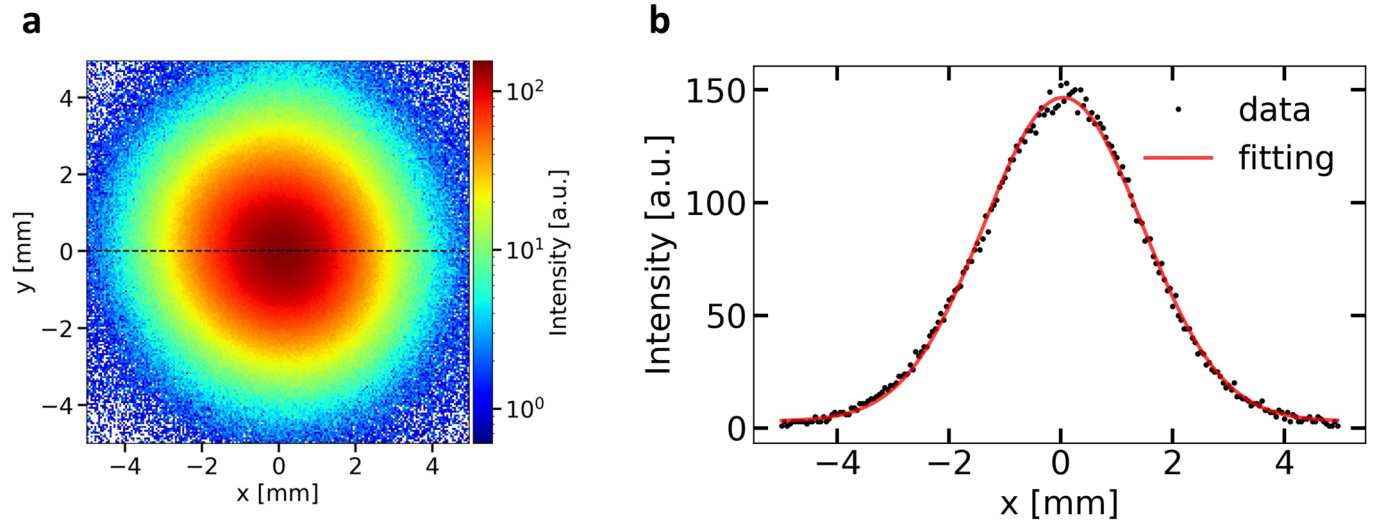


Extended Data Fig. 1 | Theoretical calculations of the electric field around a negative point charge under the Lorentz transformation. a, b, 2D electric field profiles around a negatively charged particle with energies of 0 and 35 MeV, respectively. Here, the absolute electric field strength is shown by the color bar and the direction is denoted by the black vectors.



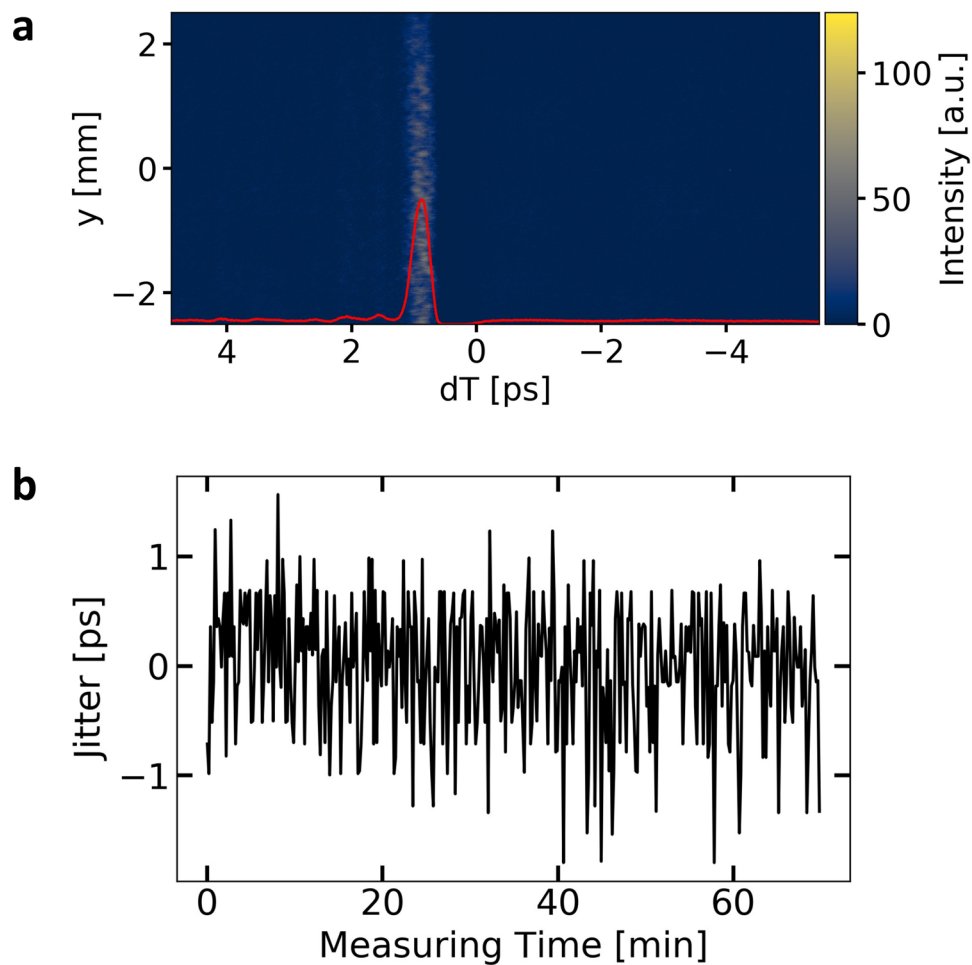
Extended Data Fig. 2 | Numerical convolution between the Gaussian profile and the electric field profile around a relativistic point charge. a, A 2D density profile of a Gaussian beam in the xz -plane ($\rho(r,t)$ at $y=0$) defined by Eq. (2). Here, we used the experimentally obtained beam sizes: beam diameter of 3.5 mm and pulse width of 0.72 ps (FWHM). **b,** A 2D electric field profile ($E_{\text{point}}(R,t)$ in the x -direction at $y=0$) around a point charge (infinitesimal electron beam)

constantly moving in the z -axis positive direction with an energy of 35 MeV. Here, the calculation box (discrete space: $550 \times 550 \times 120$) is set relatively larger than its counterpart in Fig. 2b because the boundary of the box can cause an error in the convolution. Therefore, we cropped the convoluted image and show the central part in Fig. 2b.



Extended Data Fig. 3 | Transverse beam size. **a**, An image of the fluorescence generated by injecting a relativistic electron bunch into a scintillator. This fluorescence is proportional to the density profile of the electron bunch. The transverse electron beam profile shows axial symmetry around the z-axis. **b**,

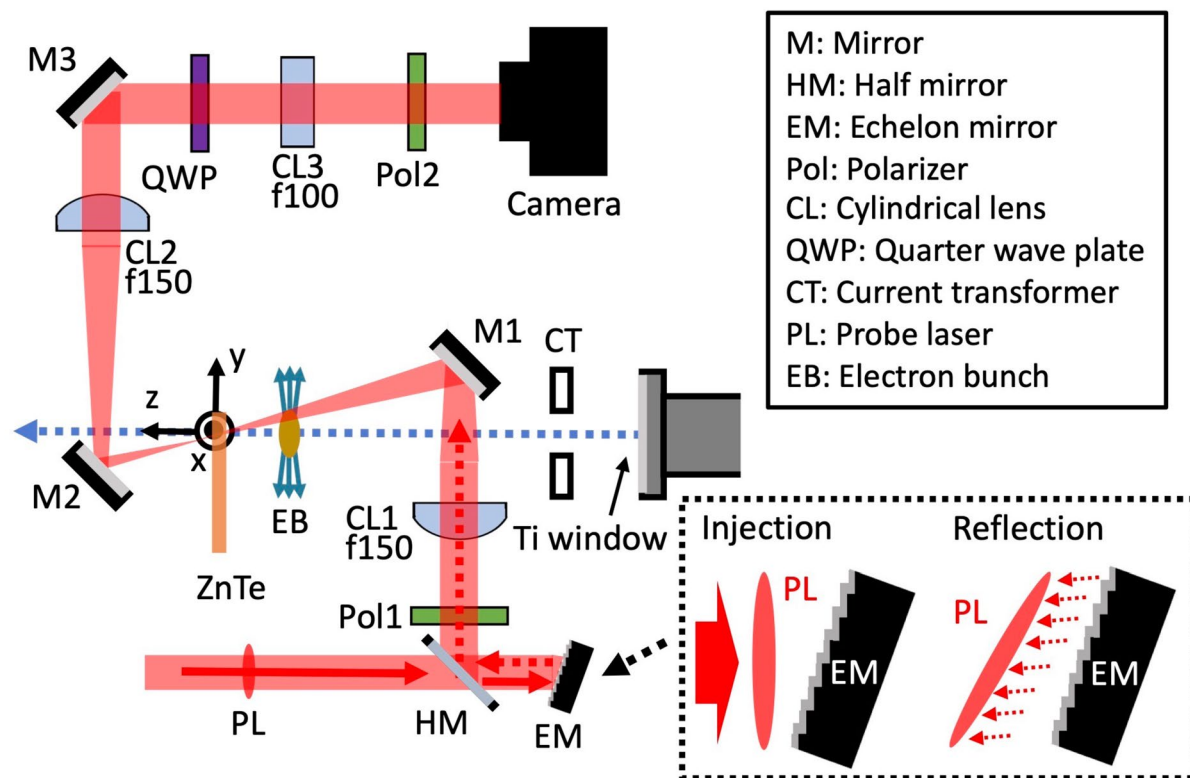
A horizontal lineout of the electron density profile obtained across the black dashed line in **a**. Black circles are the data points; this profile is fitted with a Gaussian function (red curve), and the beam size (diameter) is estimated as 3.5 mm (FWHM).



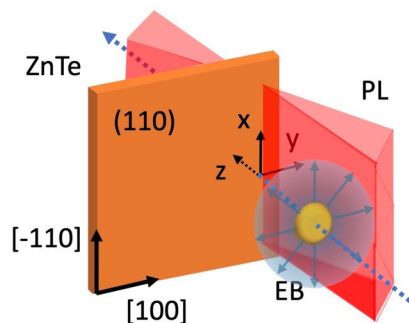
Extended Data Fig. 4 | Timing jitter between the electron beam and the probe pulse. a, A typical signal of the spatial-decoding taken by a CCD camera. The horizontal axis corresponds to the difference in the arrival time on the ZnTe

between the electron beam and the probe pulse. **b**, Arrival time difference, i.e., timing jitter, consecutively obtained for ~1 h (391 shots in total). The RMS of the timing jitter was 0.43 ps.

a

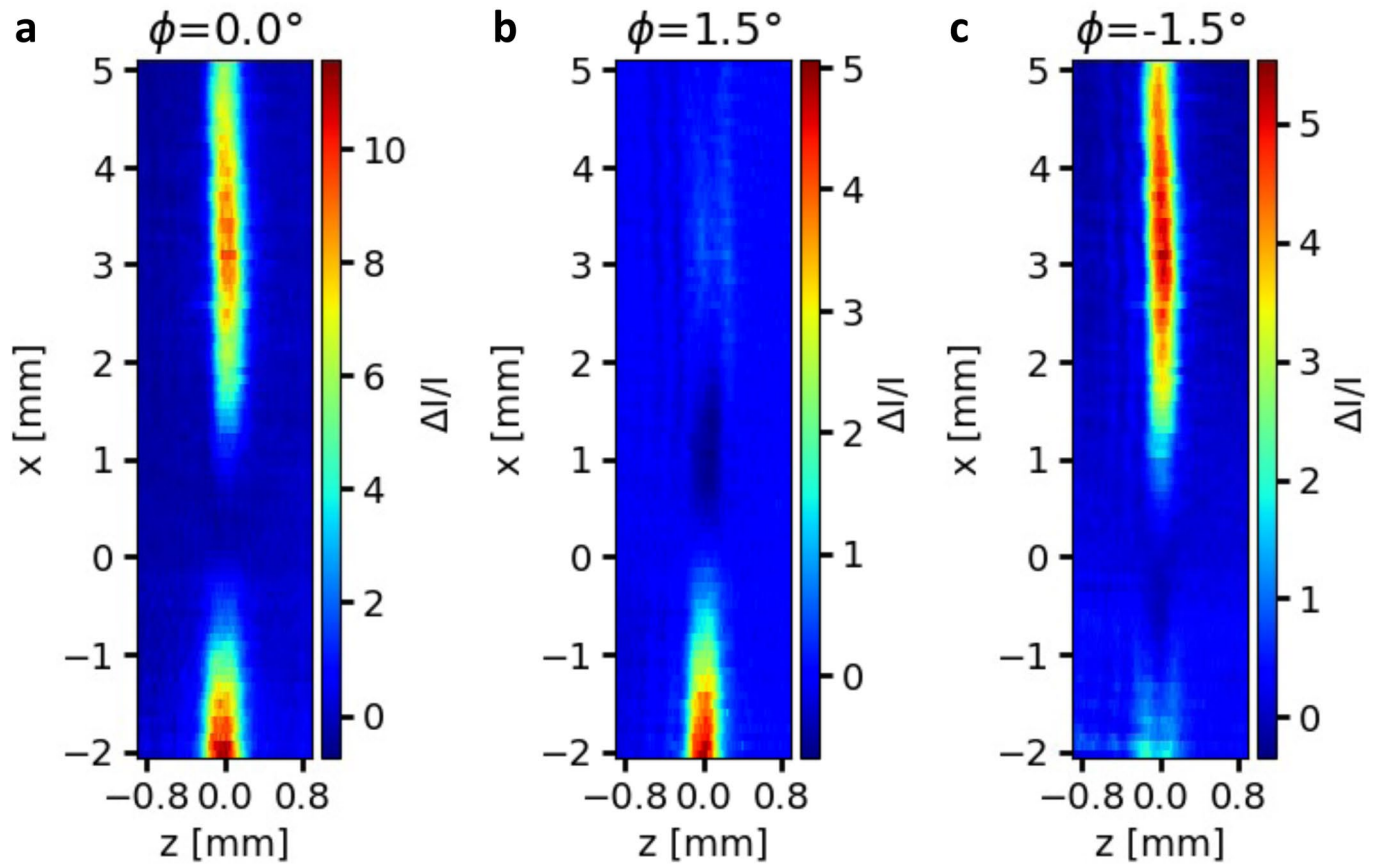


b



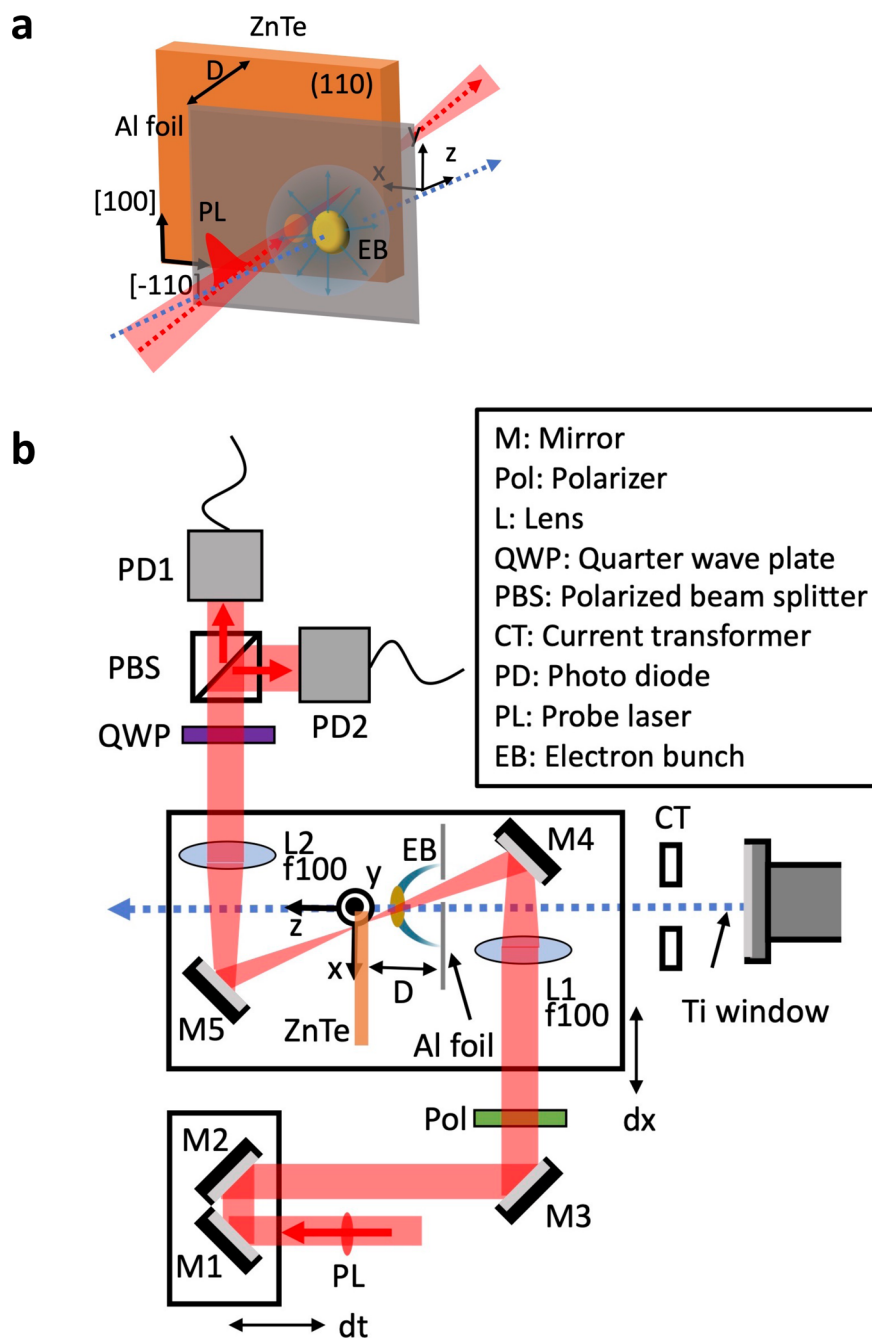
Extended Data Fig. 5 | Experimental setup of echelon-based single-shot measurement. **a**, A 2D schematic of the experimental setup. Abbreviations describing the setup are listed in the upper-right corner. Time delay is spatially imprinted on the probe laser by an echelon mirror; this imprinting converts a probe pulse to beamlets. Notably, each delay corresponds to the double length of the step height of the echelon mirror, as shown in the magnified images around the mirror in the black dashed rectangle. Red solid and dashed arrows denote the path of the probe laser before and after the reflection, respectively. The CL1 focuses the parallel beamlets into a line in the x-direction on the ZnTe, and the CL2 makes them parallel again. The distance between the CL1 and the echelon

mirror is its focal length to suppress the divergence due to the step-like mirror surface. The CL3 is rotated 90° with respect to the CL1 and CL2 for imaging in the y-direction. Here, the magnifications in the x- and y-directions are 2.8 and 1.0 on the CCD camera, respectively. The relative angle between the Pol1 and Pol2 is 90° . We used the phase offset method by rotating the QWP. The incidence angle of the probe laser into the ZnTe was 25° , whereas the electron beam path was perpendicular. **b**, A 3D schematic around the ZnTe crystal before the electron beam hits the crystal. The PL is linearly focused on the crystal by the cylindrical lens. The polarization of the PL and the measured electric field are directed in the x-direction, which corresponds to the [-110] crystal axis.



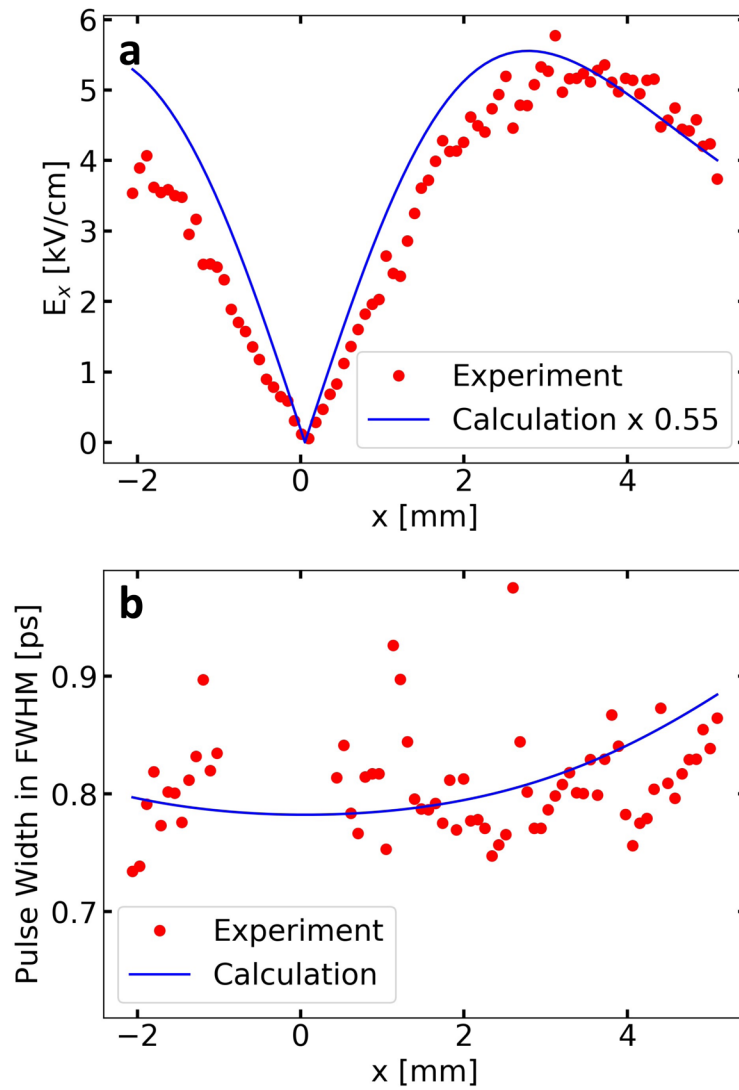
Extended Data Fig. 6 | Results of the echelon-based single-shot measurement. a–c. Spatiotemporal profiles of the electric field around a relativistic electron beam obtained through echelon-based single-shot measurement with phase offset $\phi=0^\circ$, $+1.5^\circ$, and -1.5° . The color bar denotes the

EO signal: $\Delta I = (I(\phi, \Gamma) - I(\phi, 0)) / I(\phi, 0)$. Here a corresponds to the crossed-Nicol configuration. Figure 2b shows the difference in the signal between **b** and **c**, i.e., the electric field profile obtained by the phase offset method.



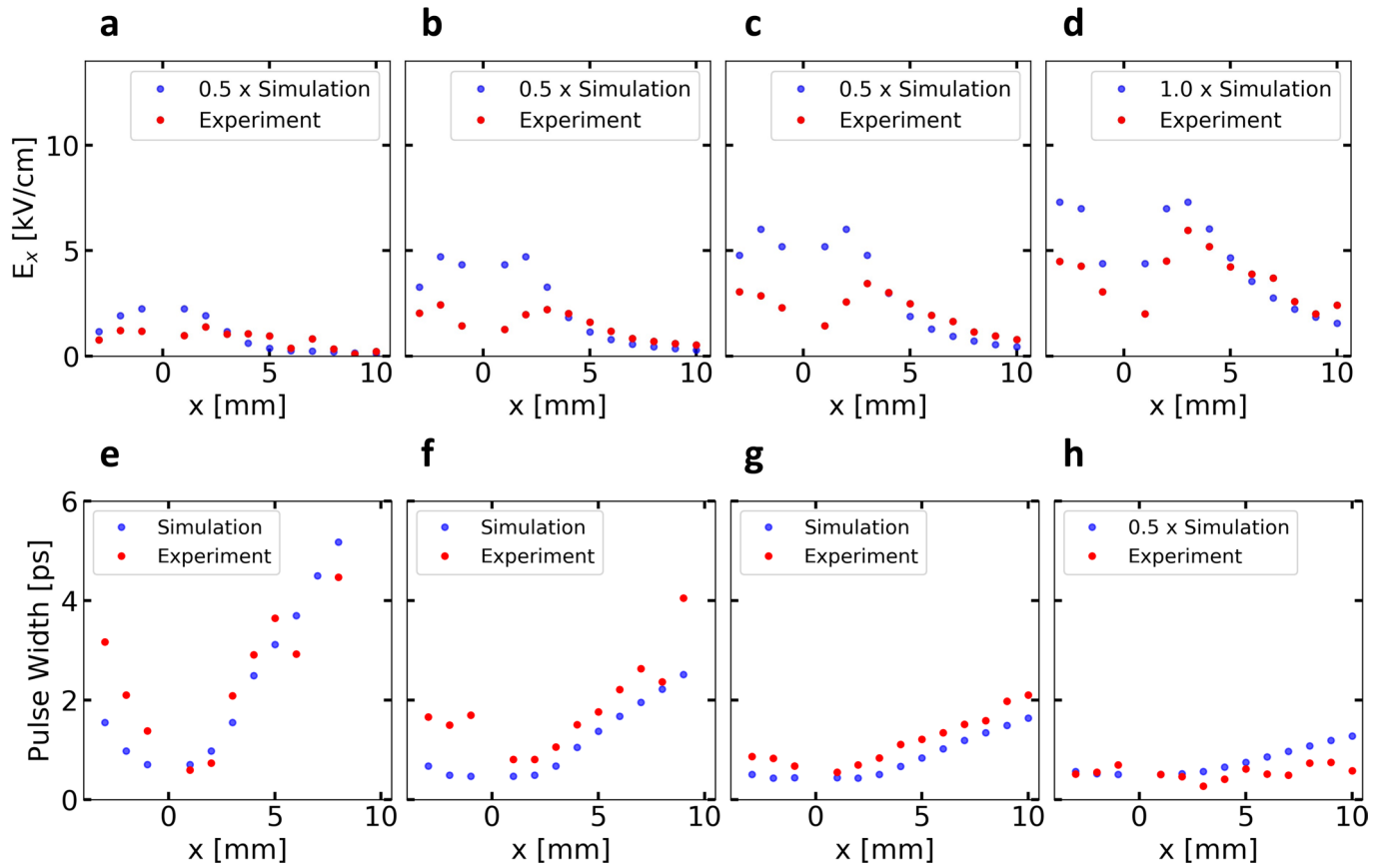
Extended Data Fig. 7 | Experimental setup used to measure the spatiotemporal evolution of the spherical electromagnetic wavefront. a, A 3D schematic around the ZnTe crystal. The focused probe pulse passed through the hole with the diameter of 1 mm in the Al foil and was incident on the crystal with an incidence angle of 37° while the electron beam passed through the Al foil. **b**, A 2D schematic of the experimental setup. Abbreviations describing the setup are listed in the upper-right corner. The probe laser was focused on the ZnTe crystal by a lens, and the transverse electric field on the spot was measured.

The polarization of the probe pulse was directed along the x-axis, and the QWP was adjusted to divide the probe pulse into two (p- and s-polarization) pulses with the same intensities. The spatiotemporal profile of the electric field was measured by moving two motorized stages for shifting the optics around the ZnTe crystal and the delay stage, respectively; they are surrounded by black rectangles in the figure, and the two-way arrows show the moving direction (dx and dt). The position of the Al foil was moved in the z-direction, and the distance D was adjusted.



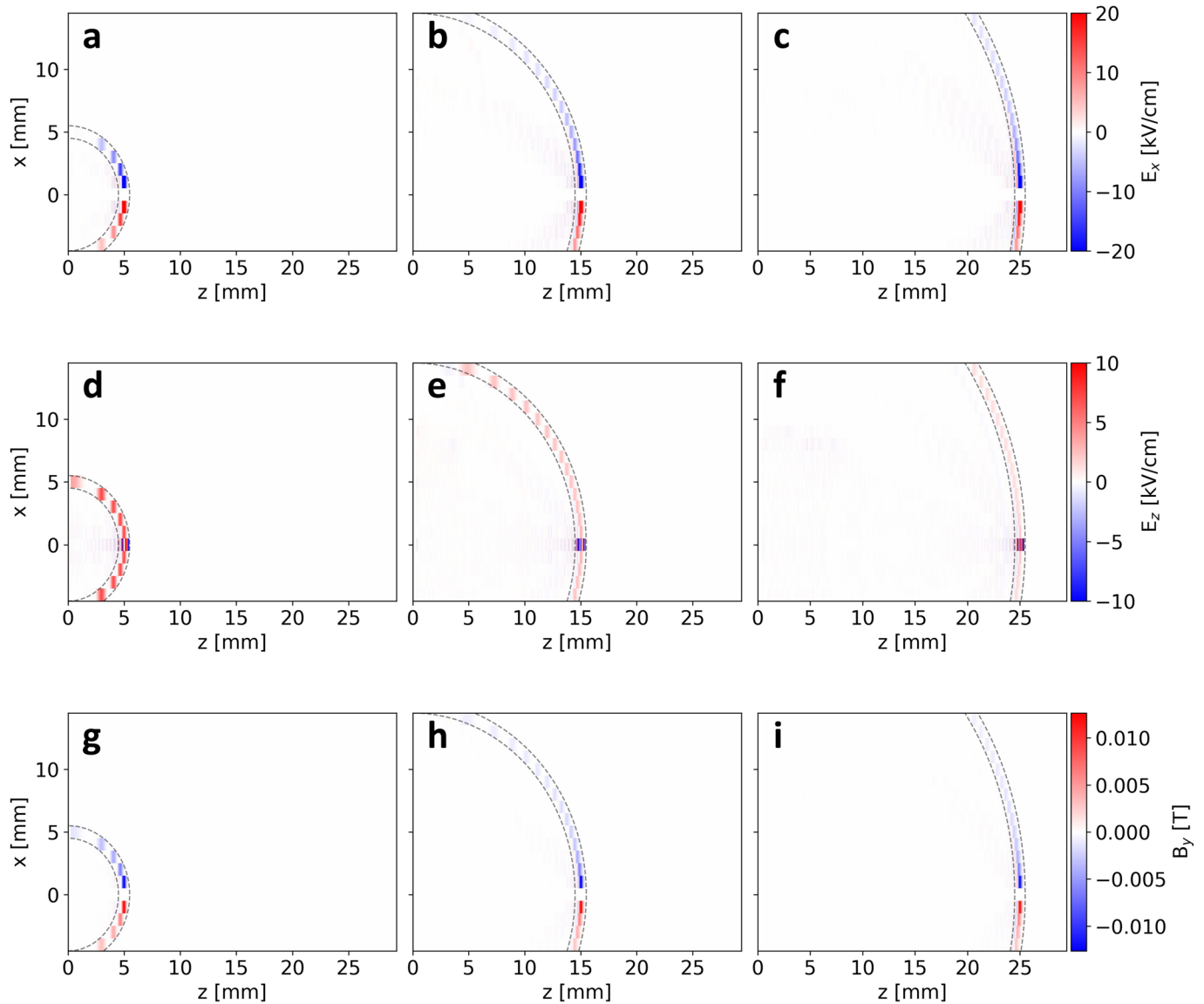
Extended Data Fig. 8 | Comparison of the electric field strength and the pulse broadening between the experiment and the calculation. a, Transverse electric field strength (E_x) of the experiment and calculation in the radial direction (x -axis). **b,** Pulse-width broadening in the radial direction. Red solid circles and blue curves denote the result of the experiment and the calculation given by the convolution between the beam profile in three dimensions and

the transverse electric field around a relativistic electron, respectively. Some experimental data points around the beam axis in the pulse broadening result are excluded because of the worse signal-to-noise ratio. Notably, the pulse width of the THz electric field (~ 0.79 ps) at $x=0$ mm is larger than the counterpart of the longitudinal beam size (~ 0.72 ps) in this energy region (35 MeV), as shown in **b**.



Extended Data Fig. 9 | Comparing the strength profile and the pulse broadening of the electric field in the radial direction around the electron beam, as obtained from the experiment and the simulation. a–h. The electric field strength profile (a–d) and pulse broadening (e–h) in the radial direction for the propagation distances of 5, 15, 25, and 209 (=D) mm after the cancellation of the electric field. Blue and red solid circles denote the simulation and experimental results, respectively. The results in a–c and e–g show a good coincidence between the results of the experiment and those of the PIC

simulation. The difference of the electric field strength between the experiment and the simulation in a–c is confirmed (see Section 6). However, the tendency observed in d differs from the other subfigures (i.e., a–c): the compensation factor changes from 0.5 to 1.0. In addition to that, the compensation factor is introduced in h. This difference arises mainly because the results d and h are obtained in a cylindrical coordinate instead of the 3D coordinate and also because of the numerical Cherenkov radiation caused by the long propagation distance, or long simulation time.



Extended Data Fig. 10 | Snapshots of the electromagnetic field around a relativistic electron beam with an infinitesimal diameter acquired by the PIC simulation. a–i, 2D transverse (a–c) and longitudinal (d–f) electric fields (E_x , E_z), and a magnetic field circulating around the beam axis ($x=y=0$) (g–i) (B_y) in the xz -plane at the time when an electron beam with an infinitesimal diameter,

a pulse width of 1.0 ps (FWHM), an energy of 35 MeV, and a charge amount of 70 pC propagates for 5, 15, and 25 (=D) mm after the metallic boundary ($z=0$ mm), as obtained by the PIC simulation. The black dashed lines are part of a sphere with a radius of $D-0.5$ and $D+0.5$ mm.